Journal of
Materials Chemistry A

ROYAL SOCIETY
OF CHEMISTRY

PAPER

View Article Online
View Journal | View Issue

Check for updates

Cite this: *J. Mater. Chem. A*, 2024, **12**, 29802

The switchable bulk photovoltaic effect in 2D room temperature ferroelectric $CuInP_2S_6$†

Chengwei Liao,[a] Minglong Wang[a] and Yu-Jun Zhao *[ab]

Received 16th May 2024
Accepted 23rd September 2024

DOI: 10.1039/d4ta03402c

rsc.li/materials-a

The bulk photovoltaic effect (BPVE) is a crucial branch of nonlinear optics that plays a significant role in fundamental physics and practical applications. In this study, we have investigated the BPVE of a room-temperature ferroelectric material $CuInP_2S_6$ (CIPS) through first-principles calculations and nonlinear response theory. It is revealed that there are significant differences in nonlinear photo-responsivity among the ferroelectric, paraelectric, and antiferroelectric phases under monochromatic light. We find that the nonlinear photocurrent can be switched by the chirality of the incident light, depending on the structural symmetry. Using the CI-NEB method, we have studied the evolution of photocurrent during phase transition processes such as polarization reversal and polar-to-nonpolar transitions. We observe that the reversal of ferroelectric ordering can induce a photocurrent flip, attributed to the sign change of topological physical quantities such as the shift vector and Berry curvature. Furthermore, we predict the modulation of photocurrent through chalcogen element substitution and strain engineering. Our study provides an insight into the nonlinear optics of ferroelectric materials and crucial theoretical guidance for the design of optoelectronic and photonic devices.

1. Introduction

In recent years, the study of nonlinear optics with topological quantities, such as the shift vector and Berry curvature, has attracted significant research interest, along with the development of topology. Understanding the interaction between light and matter is fundamental for optics and optoelectronics. The second-order nonlinear optical response includes the bulk photovoltaic effect (BPVE)[1–3] and second harmonic generation (SHG),[4,5] where 'nonlinear' implies a non-linear relationship between photo-induced charge polarization and the optical field. In contrast to traditional p–n junctions, the BPVE can generate a photovoltaic effect without the need for special interface structures and can produce an open-circuit voltage greater than the inherent band gap,[6] with the conversion efficiency potentially exceeding the Shockley–Queisser limit.[7] This property renders the BPVE promising for applications in energy harvesting,[8] photodetection,[9] structural characterization,[10,11] *etc.* The phenomenon of BPVE necessitates the disruption of spatial inversion symmetry, also known as *P*-symmetry, within the system, as this symmetry causes polar vectors (polarization and electric fields) to undergo a reversal. Ferroelectric materials, with spontaneous displacements of positive/negative ions, naturally break *P*-symmetry, rendering them hot materials for nonlinear optical response studies.[12–15]

Ferroelectric materials exhibit spontaneous charge polarization, where the displacement of positive and negative ions causes macroscopic polarization. Under external stimuli, reversible polarization reversal can be achieved. In traditional ferroelectric materials, such as perovskite oxides, a reduction in thickness will enhance the depolarizing field, and the ferroelectricity will disappear when the thickness is below a critical value.[16–18] For example, the perovskite oxide $BaTiO_3$ becomes an ordinary semiconductor when its thickness is less than six unit cells.[17] With the development of two-dimensional (2D) materials, studies have found that 2D ferroelectric materials may also exist. The intrinsic ferroelectricity is strong enough to counteract the depolarizing field, allowing ferroelectricity to be preserved in the 2D form. So far, common in-plane ferroelectric materials include MX, with M = (Ge, Sn) and X = (S, Se),[19] and group-V (As, Sb, and Bi) single elements,[20] and out-of-plane ferroelectric materials include $1T'$-WTe_2,[21] α-In_2Se_3,[22] M_2X_3 (M = Al, Ga, In; X = S, Se, Te),[23] *etc.* Recently, it has been experimentally discovered that thin layers of $CuInP_2S_6$ (CIPS) are room-temperature ferroelectric materials,[24,25] and the monolayer has a van der Waals layered structure. In the monolayer, the metal atoms Cu and In induce out-of-plane charge polarization through vertical displacement, exhibiting robust

---

[a] *Department of Physics, South China University of Technology, Guangzhou 510641, China. E-mail: zhaoyj@scut.edu.cn*

[b] *Key Laboratory of Advanced Energy Storage Materials of Guangdong Province, South China University of Technology, Guangzhou 510641, China*

† Electronic supplementary information (ESI) available: Details of formula derivation, structural symmetry and non-zero conductivity tensors, photoconductivities of CIPS in different ferroic phases, CI-NEB path of phase transitions, evolution of photocurrents and physical quantities during phase transitions, photoconductivities of CIPX (X = S, Se, Te), and photoconductivities under biaxial strain. See DOI: **https://doi.org/10.1039/d4ta03402c**

ferroelectricity at room temperature. CIPS exhibits remarkable ferroelectric properties, endowing it with significant potential for technological applications, such as in non-volatile memory devices,[26] field-effect transistors,[27] and photocatalysis.[28] Despite the rapid advancement of research on 2D ferroelectric materials, the microscopic origins of the BPVE, as well as the coupling between nonlinear photocurrent and ferroelectric order in ferroelectric materials, remain poorly understood. Moreover, the development of effective methods to manipulate nonlinear photocurrent is crucial for practical applications.

In this study, we have employed first-principles calculations to explore the BPVE in the 2D ferroelectric material CIPS. We have conducted an analysis of the structural symmetries associated with various ferroic phases of the CIPS material, which include ferroelectric, paraelectric, and antiferroelectric phases. The photocurrent conductivity tensor is calculated for these phases within the context of the BPVE. The evolution of photocurrent during phase transition processes is also studied, such as polarization reversal and polar-to-nonpolar transitions. Additionally, we propose effective strategies for modulating the photocurrent, including chalcogen element substitution (CIPX; X = S, Se, Te) and strain engineering.

2. Theory and formulas of the BPVE

When monochromatic light is shone on a system with broken *P*-symmetry, the BPVE can directly convert light into direct current (DC). According to the quadratic Kubo response theory,[29,30] we can treat the light interaction as a perturbation. Implementing the density matrix approach, under the independent particle approximation, the second-order nonlinear photocurrent density in the velocity gauge can be written as follows:[13,31–33]

$$J^a_{bc} = -\frac{e^3}{\hbar^2\omega^2}\mathrm{Re}\left\{\sum_{m,n,l}^{\Omega=\pm\omega}\int_{BZ}\frac{\mathrm{d}^3\boldsymbol{k}}{(2\pi)^3}f_{lm}\frac{v^b_{lm}}{\omega_{ml}-\Omega+i/\tau}\left(\frac{v^a_{mn}v^c_{nl}}{\omega_{mn}+i/\tau}-\frac{v^c_{mn}v^a_{nl}}{\omega_{nl}+i/\tau}\right)E_b(\Omega)E_c(-\Omega)\right\} \tag{1}$$

Under different polarized light illumination, the photocurrent can be separated into two components: shift current (SC) induced by linearly polarized light (LPL) and injection current (IC) induced by circularly polarized light (CPL), which is also known as circular photocurrent or ballistic current. Here, we primarily focus on the photoconductivity of the photocurrent, as knowing only the frequency and intensity of the incident light allows us to obtain the photocurrent:[11,13,33]

$$J^a_{\mathrm{SC}} = 2\sigma^a_{bc}(0;\omega,-\omega)E_b(\omega)E_c(-\omega) \tag{2}$$

$$\frac{\mathrm{d}\left(J^a_{\mathrm{IC}}\right)}{\mathrm{d}t} = 2\eta^a_{bc}(0;\omega,-\omega)E_b(\omega)E_c(-\omega) \tag{3}$$

where a, b, and c are Cartesian indices, the superscript a denotes the direction of the photocurrent, and the subscripts b and c denote the direction of the electric field of the incident light. σ^a_{bc} (η^a_{bc}) is the photoconductivity of the SC (IC). E_b and E_c are the Fourier components of the electric field, $\boldsymbol{E}(t) = \boldsymbol{E}(\omega)\mathrm{e}^{-i\omega t} + \boldsymbol{E}(-\omega)\mathrm{e}^{i\omega t}$, and the angular frequency of the incident light is ω.

In systems where the *P*-symmetry is broken while the time-reversal symmetry (*T*-symmetry) is preserved, $Tv_{mn}(\boldsymbol{k}) = -v^*_{mn}(-\boldsymbol{k})$, where * indicates the complex conjugate, so eqn (1) can be simplified further. In eqn (1), $Tv_{mn}v_{nl}v_{lm} = -(v_{mn}v_{nl}v_{lm})^*$, implying that the real and imaginary parts of the numerator are odd and even functions in the $\boldsymbol{k}$-space, respectively. Therefore, only the imaginary part of the numerator contributes to the total conductivity when integrating over the entire first Brillouin zone (BZ). Moreover, the denominator is invariant under *T*-symmetry. The DC current must be a real quantity, and there is no phase difference between the electric fields E_b and E_c for LPL, so SC must consider the imaginary part of the denominator, and there is a phase difference i between the electric fields for CPL, so IC needs to consider the real part of the denominator. Thus, the photoconductivity for SC and IC in length gauge can be written as follows (a more detailed derivation of the formula can be found in the ESI†):

$$\sigma^a_{bc} = -\frac{i\pi e^3}{2\hbar^2}\int_{BZ}\frac{d^3\boldsymbol{k}}{(2\pi)^3}\sum_{m,n}f_{nm}\left(r^b_{mn}r^c_{nm;a}+r^c_{mn}r^b_{nm;a}\right)\delta(\omega_{mn}-\omega) \tag{4}$$

$$\eta^a_{bc} = \frac{\pi e^3}{2\hbar^2}\int_{BZ}\frac{d^3\boldsymbol{k}}{(2\pi)^3}\sum_{m,n}f_{nm}\Delta^a_{nm}\left[r^b_{mn}, r^c_{mn}\right]\delta(\omega_{mn}-\omega) \tag{5}$$

where m and n are band indices, and $\boldsymbol{k}$ is omitted from all k-dependent physical quantities for brevity, *e.g.* $r^a_{mn}(\boldsymbol{k})$. $f_{nm} = f_n - f_m$ and $\hbar\omega_{mn} = E_m - E_n$ are the electrons occupied and the energy difference between bands n and m, respectively. $r^a_{mn} = \frac{v^a_{mn}}{i\omega_{mn}}$ ($m \neq n$) is the interband Berry connection and $v^a_{mn} = \left\langle m\middle|\frac{\mathrm{d}H}{\mathrm{d}k_a}\middle|n\right\rangle$ is the interband velocity matrix. The gauge covariant derivative for r^b_{nm} is $r^b_{nm;a} == \frac{\partial r^b_{nm}}{\partial k_a} - ir^b_{nm}(A^b_{nn} - A^b_{mm})$, where A^a_{nn} is the intraband Berry connection. The group velocity difference is $\Delta^a_{nm} = v^a_{nn} - v^a_{mm}$. The commutative relation between Berry connections is $[r^b_{mn},r^c_{nm}] = r^b_{mn}r^c_{nm} - r^c_{mn}r^b_{nm}$.

In order to have a more intuitive understanding of the physical mechanisms of SC and IC, by simply transforming the conductivities, they can be written in a more popular and cleaner form:

$$\sigma^a_{bb} = -\frac{\pi e^3}{2\hbar^2}\int_{BZ}\frac{d^3\boldsymbol{k}}{(2\pi)^2}\sum_{m,n}f_{nm}R^{a,b}_{nm}\left|r^b_{mn}\right|^2\delta(\omega_{mn}-\omega) \tag{6}$$

$$\eta^{a}_{bc} = \frac{\pi e^{3}}{2\hbar^{2}} \int_{BZ} \frac{\mathrm{d}^{3}\boldsymbol{k}}{(2\pi)^{3}} \sum_{m,n} f_{nm} \varDelta^{a}_{nm} \varOmega^{bc}_{mn} \delta(\omega_{mn} - \omega) \tag{7}$$

where for SC photoconductivity, $R^{a,b}_{nm}$ is the topological physical quantity shift vector, $R^{a,b}_{nm} = \frac{\partial \phi^{b}_{nm}}{\partial k_{a}} - A^{a}_{nn} + A^{a}_{mm}$, $r^{b}_{nm} = |r^{b}_{nm}| e^{i\phi_{mb}{}^{n}}$, ϕ^{b}_{nm} is the phase factor of r^{b}_{nm}, and the optically excited transition rate is $|r^{b}_{nm}|^{2} = r^{b}_{nm} r^{b}_{mn}$. For IC photoconductivity, $\varDelta^{a}_{nm}$ is the velocity difference and $\varOmega^{bc}_{mn} = [r^{b}_{mn}, r^{c}_{nm}]$ is the topological physical quantity Berry curvature. The Dirac delta function $\delta(\omega_{mn} - \omega)$ represents the light-induced resonance interband transition of carriers when the incident light satisfies $\omega = \omega_{mn}$. Eqn (6) and (7) are widely applied in multiple articles.[31–33] We can get facts from eqn (6) and (7) that the SC originates from the carrier wave packet shifts under optical excitation, wavefunction centers between electrons and holes have a phase difference R^{a}_{nm}, which produces an electric dipole, and the time derivative of the electric dipole is the current. The IC originates from the asymmetric transport of carriers under optical excitation, where electrons and holes are excited with different velocities and unbalanced motions, resulting in a net current.

Before numerical calculations, some specific clarifications need to be provided. The SC is a static current that is independent of the carrier lifetime τ. Under light irradiation, the current is instantaneously generated as long as the incident light energy exceeds the material's band gap. The IC initially grows with time and reaches saturation in the static limit. Therefore, the effective photoconductivity of IC should be defined as $\tau\eta^{a}_{bc}$. In this study, we approximate the carrier relaxation time using a small conservative constant of 0.2 ps,[13,32,33] considering that theoretically and experimentally measured semiconductor carrier lifetimes are generally greater than this value, such as the carrier lifetime of MoS_2 is $\tau \sim 2$ ps[34] and that of the thin-film topological insulator Bi_2Se_3 is $\tau \sim 1$ ps at room temperature.[35] In practical situations, the carrier lifetime varies at different energy bands and $\pm\boldsymbol{k}$ points; here, we treat it as a constant, which does not affect the qualitative characteristics of theoretical calculations. Furthermore, to validate the accuracy of our photoconductivity calculation program, we replicated previous research by computing the photoconductivity of 2D 2H-MoS_2, and calculation results are found to be consistent with previous findings,[32] as illustrated in ESI Fig. S1(a) and (b).† Lastly, the computed results for photoconductivity using the velocity gauge and length gauge formulas are identical since they analyze the same physical effects;[36,37] we calculated the conductivity under both gauges, which are also shown in Fig. S1(a) and (b).†

3. Results and discussion

3.1 The atomic and electronic structures of CIPS

The top and side views of the atomic structure of the 2D room-temperature ferroelectric material CIPS are shown in Fig. 1(a) and (b), respectively. The Cu and In atoms, along with the vertically oriented P–P atoms, are all located within a framework formed by six S atoms. The upper and lower three S atoms exhibit a relative rotation of 60°, as indicated by the shaded region in Fig. 1(a). Fig. 1(b) illustrates the side views of the structural configurations of the ferroelectric (FE1/FE2) phases, the paraelectric (PE) phase, and the antiferroelectric (AFE) phase in CIPS. In the FE1 (FE2) phase, Cu atoms undergo upward (downward) displacement along the direction

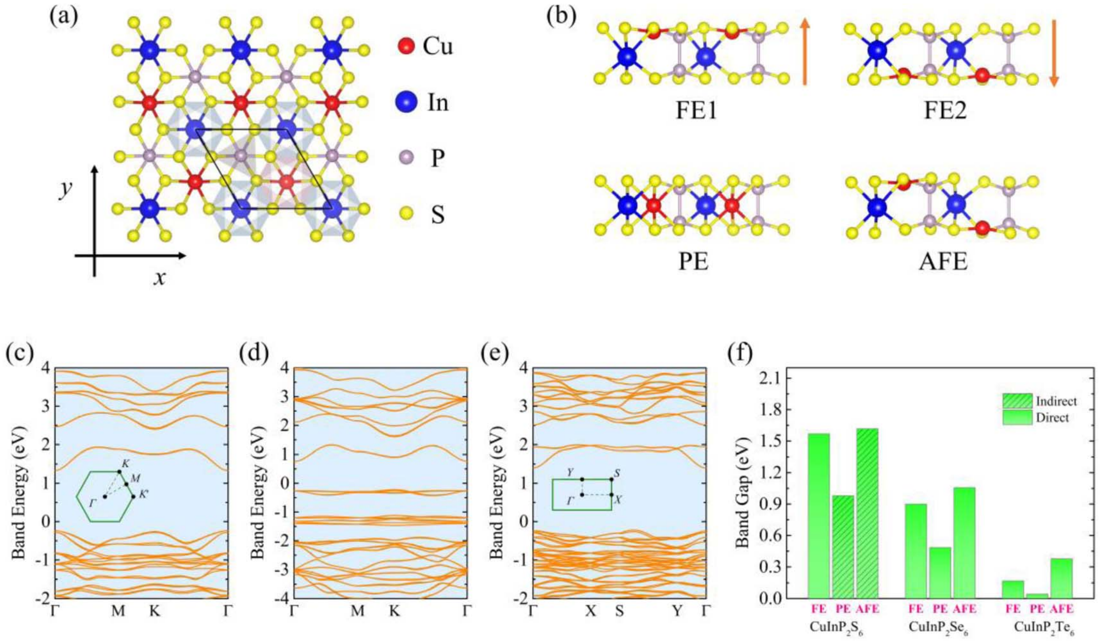

Fig. 1 The atomic and electronic structures of CIPS. (a) and (b) the top and side views of the CIPS structure. (c)–(e) The band structures of CIPS in the FE1/FE2, PE, and AFE phases, with insets showing the first Brillouin zone. (f) The band gaps of CIPS, CIPSe, and CIPTe in different phases, with shaded markings indicating the indirect band gap.

perpendicular to the plane, while In atoms exhibit a slight downward (upward) movement, resulting in charge polarization with the direction indicated by the orange arrows in the figure. In the PE phase, Cu and In atoms are positioned at the middle of the atomic layer. In the AFE phase, adjacent Cu atoms undergo displacements in opposite directions. In both the PE and AFE phases, ferroelectric properties are absent.

To verify the structural stability of the FE1, FE2, PE, and AFE phases of CIPS, we calculated their phonon spectra, as shown in Fig. S2.† We found that the phonon spectra of FE1, FE2, and AFE phases do not exhibit any imaginary frequencies, indicating that they possess good dynamical stability. In contrast, the PE phase exhibits imaginary frequencies in its phonon spectrum, suggesting that the positions of Cu and In atoms in the middle of the atomic layers are detrimental to its structural stability. In the structure after full relaxation, the lattice constants for the FE1/FE2, PE, and AFE phases are found to be 6.16 Å, 6.10 Å, and 6.17 Å, respectively. These values are consistent with previous research,[38,39] and the lattice constants as well as the energy differences between different phases are presented in ESI Table S1.† In addition, we have compared the energy differences between different phases $\Delta E_1 = E_{\mathrm{PE}} - E_{\mathrm{FE}} = 326.2$ meV and $\Delta E_2 = E_{\mathrm{FE}} - E_{\mathrm{AFE}} = 51.3$ meV. Theoretical calculations indicate that the ground state structure is the AFE phase,[39,40] and the energy difference between FE and AFE phases is very small. Under the external field, the phase transition between FE and AFE can be easily achieved.[39–41]

Fig. 1(c)–(e) illustrate the band structures of the FE1/FE2, PE, and AFE phases, respectively, in CIPS. FE1 and FE2 exhibit identical band structures with a band gap of 1.57 eV. The valence band maximum (VBM) and conduction band minimum (CBM) are both located at the high symmetry point Γ, indicating a direct band gap semiconductor. The PE and AFE transform into indirect band gap semiconductors, with band gaps of 0.98 eV and 1.62 eV, respectively. In the PE phase, the VBM is located at the K point, while in the AFE phase, the VBM is situated along the S–Y high symmetry line, and the CBM is situated at the Γ point for both phases. It is worth noting that in the AFE phase, the positions of two adjacent Cu atoms are different. The first Brillouin zone of the AFE phase is a rectangle, as shown in the inset of Fig. 1(e). By calculating the projected band structures of the CIPS FE phase, we analyzed the atomic orbital distribution near the Fermi level, as shown in Fig. S3.† The VBM is primarily contributed by Cu 3d and S 3p, while the CBM is mainly from In 5s, P 3s and S 3p.

For the practical diversification of the system, we further considered the replacement of S atoms with Se and Te atoms, such as structures $\mathrm{CuInP_2Se_6}$ (CIPSe) and $\mathrm{CuInP_2Te_6}$ (CIPTe). To verify the dynamical stability of the structures after chalcogen element substitution, we calculated the phonon spectra of CIPSe and CIPTe, as shown in Fig. S4.† We observed that the phonon spectra of the FE phases of CIPSe and CIPTe do not exhibit any imaginary frequencies, indicating good dynamical stability. The lattice constants and energy differences of CIPSe and CIPTe are provided in Table S1,† and the band structures are illustrated in Fig. S5.† Fig. 1(f) presents the band gap of the FE, PE, and AFE phases for CIPS, CIPSe, and CIPTe; except for PE and AFE of CIPS, all other phases behave as direct band gap semiconductors. In this system, the band gap ranges from 0.04 to 1.62 eV, with the smallest gap in the PE phase and the largest in the AFE phase. In the PE phase, both Cu and In atoms are positioned in the middle of the atomic layers, making the PE phase structurally unstable. As shown in Fig. S5,† the band structure of the PE phase of CIPX (X = S, Se, and Te) exhibits four relatively localized valence bands. The localized valence bands near the Fermi level in the unstable PE phase result in its smallest band gap. Through elemental substitution, S to Se and Te, the band gap gradually decreases, with the smallest gap of 41.7 meV being observed in the PE phase of CIPTe.

3.2 The BPVE in the room temperature ferroelectric phase

Before discussing the BPVE in the 2D room temperature ferroelectric material CIPS, we first need to analyze the symmetry of the CIPS structure and the independent non-zero conductivity tensor. The FE1 and FE2 phases possess identical symmetries, although their polarization directions are opposite. Their space group is $P3$ (No. 143), and the point group is C_3, as illustrated in Table S2.† In the FE1/FE2 phase, there is a three-fold rotational symmetry axis perpendicular to the plane denoted by yellow arrows, with three symmetry operations $C_3^{(1)}$, $C_3^{(2)}$and $C_3^{(3)}$ represented by black diamonds. The PE phase space group is $P312$ (No. 149), and the point group is D_3. Due to Cu and In atoms located at the middle of the atomic layer, the symmetry of the PE phase is higher compared to that of the FE phase. In the PE phase, in addition to a perpendicular three-fold rotational symmetry axis, there are three in-plane two-fold rotational symmetry axes, with $C_2^{(1)}$, $C_2^{(2)}$ and $C_2^{(3)}$ symmetry operations denoted by green arrows. The AFE phase possesses the space group $P21$ (No. 4) and point group C_1, with only invariant operation E. Due to the opposing positions of adjacent Cu atoms, both two-fold and three-fold rotational axes vanish, resulting in the lowest symmetry for the AFE phase.

All phases in CIPS lack P-symmetry, thereby permitting second-order nonlinear optical effects. According to Boyd *Nonlinear Optics*,[42] the C_3 point group has 21 non-zero conductivity tensors, such as $xxx = -xyy$, $xzz = 0$, $yxx = -yyy$, $yzz = 0$, $zxx = zyy$, zzz and $xxy = 0$, $xyz = -yxz$, and $xzx = yzy$; all non-zero conductivity tensors are listed in Table S3.† The D_3 point group has 10 non-zero conductivity tensors. The addition of three in-plane two-fold rotational symmetries results in $xxx = xyy = xzz = 0$, $zxx = zyy = zzz = 0$, and $xzx = yzy = 0$, reducing the number of non-zero components. It is worth noting that in the D_3 point group, the traditionally defined directions differ from our work (as shown in Fig. 1(a)), where the x-axis corresponds to the traditionally defined y-axis, the y-axis corresponds to the traditionally defined x-axis, and the z-axis remains the same. Generally, higher symmetry implies more symmetry operations and fewer non-zero conductivity tensors. This is because certain symmetry operations can cause the current to vanish, for example, mirror M_x symmetry would make the photocurrent along the x-direction zero.[13,32]

Under LPL illumination, we computed all the SC photoconductivity tensors for CIPS in the FE1 phase, as shown in

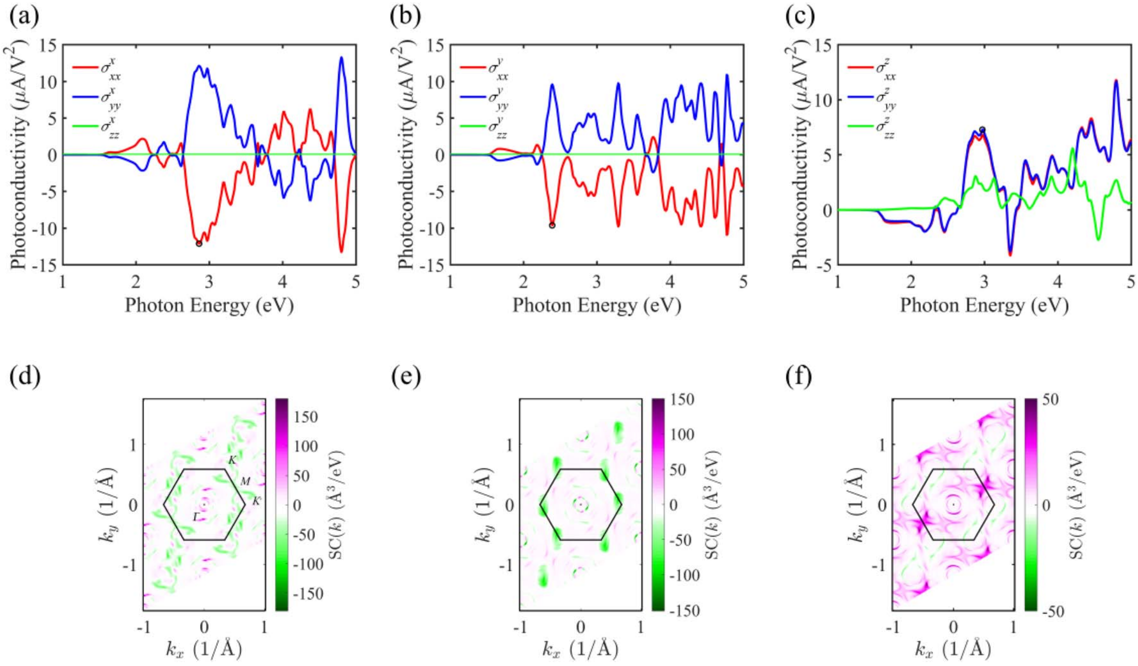

Fig. 2 The SC photoconductivities of CIPS in the FE1 phase and the $\boldsymbol{k}$-resolved SC($\boldsymbol{k}$) functions. (a)–(c) The SC photoconductivity in the x-, y-, and z-directions, respectively. (d) The SC($\boldsymbol{k}$) function of σ^x_{xx} at photon energy $\hbar\omega = 2.86$ eV. (e) The SC($\boldsymbol{k}$) of σ^y_{xx} at $\hbar\omega = 2.39$ eV. (f) The SC($\boldsymbol{k}$) of σ^z_{yy} at $\hbar\omega = 2.97$ eV.

Fig. 2(a)–(c). We observe that for the SC in the x-direction, $\sigma^x_{xx} = -\sigma^x_{yy}$ and $\sigma^x_{zz} = 0$, first-principles calculations are consistent with the previously analyzed non-zero conductivity tensor based on symmetry. The SC along the y-axis is similar to that along the x-axis, with $\sigma^y_{xx} = -\sigma^y_{yy}$. The SC along the z-axis is different from that along the x and y directions, $\sigma^z_{xx} = \sigma^z_{yy}$ and $\sigma^x_{zz} \neq 0$, as the structure belongs to the C_3 point group. Regarding the SC in the x and y directions, polarized light can switch the direction of the photocurrent, and under LPL-xx and LPL-yy the current reverses. However, in the z-direction, each component is non-zero, and polarized light cannot change the current direction. All these results are consequences of the structural symmetry constraints. The photoconductivity varies with the photon energy of the incident light, which is caused by electronic transitions between different energy bands induced by photons of varying energies. Transitions of electrons between different energy bands can result in photoconductivity being positive or negative, depending on the geometric properties of the energy bands involved in the transitions. Additionally, we observe that when the photon energy of the incident light is less than the band gap, the conductivity $\sigma = 0$. This is because we only consider interband transitions ($m \neq n$) here and do not account for intraband contributions. For the physical mechanisms of SC and IC, the intraband contribution is several orders of magnitude smaller than the interband contribution.[13,32,33]

To explore the origin of photoconductivity, we calculated the distribution of the integrated function of the SC photoconductivity in the $\boldsymbol{k}$-space, $\mathrm{SC}(k) = \mathrm{Re}\left\{ i\sum_{n,m} f_{nm}\left(r^b_{mn}r^c_{nm;a} + r^c_{mn}r^b_{nm;a}\right)\delta(\omega_{mn} - \omega)\right\}$, as shown in Fig. 2(d)–(f). Here, we investigate the conductivity peaks in the visible light range, as indicated by the black circles in the figure. Incident light $\hbar\omega = 2.86$ eV, $\sigma^x_{xx} = -12.1$ μA V^{-2}, and the main contributions of SC($\boldsymbol{k}$) come from carrier transitions near the high symmetry points Γ, K, and K', as shown in Fig. 2(d). In the y-direction, $\hbar\omega = 2.39$ eV and $\sigma^y_{xx} = -9.6$ μA V^{-2}, and the main contributions originate from the high symmetry points K and K', as illustrated in Fig. 2(e). In the z-direction, $\hbar\omega = 2.97$ eV and $\sigma^z_{yy} = 7.3$ μA V^{-2}, and the main contributions come from near the Γ point and the high symmetry point M, as shown in Fig. 2(f). We observe that the integrated function of non-zero conductivity is symmetric with respect to $\boldsymbol{k}$, indicating SC($\boldsymbol{k}$) = SC($-\boldsymbol{k}$). The distribution plots of the integrated functions in different directions show significant differences, which arise from the structural symmetry and the selective excitation of photons in different directions.

Under CPL illumination, we computed FE1 phase all IC conductivity tensors, as shown in Fig. 3(a)–(c). The computational results are consistent with the symmetry analysis mentioned above. From Fig. 3(a) and (b), we observe that $\tau\eta^x_{yz} = \tau\eta^y_{zx}$, $\tau\eta^x_{zx} = -\tau\eta^y_{yz}$, and $\tau\eta^x_{xy} = \tau\eta^y_{xy} = 0$. Interestingly, we observe that completely identical or opposite photocurrent can be generated in the x and y directions under different polarized lights (yz and zx), such as $\tau\eta^x_{yz} = \tau\eta^y_{zx}$ and $\tau\eta^x_{zx} = -\tau\eta^y_{yz}$. Furthermore, we discovered that switching the chirality of incident light CPL can reverse the direction of the photocurrent, as seen in $\tau\eta^x_{zx} = -\tau\eta^x_{xz}$ and $\tau\eta^y_{zx} = -\tau\eta^y_{xz}$. This is due to the commutative properties of Berry curvature, where $\Omega^{bc}_{mn} = r^b_{mn}r^c_{nm} - r^c_{mn}r^b_{nm} = -\Omega^{cb}_{mn}$. Such behavior represents a universal characteristic of the IC. Similar to SC, we also investigated the

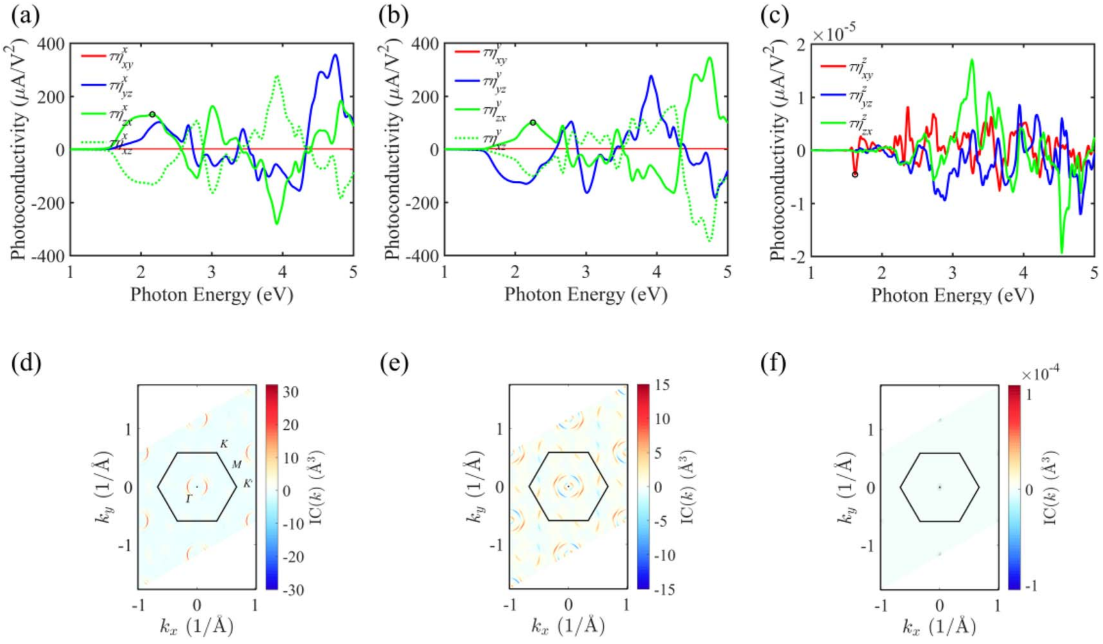

Fig. 3 The IC photoconductivities of CIPS in the FE1 phase and the $\boldsymbol{k}$-resolved IC($\boldsymbol{k}$) functions. (a)–(c) The IC photoconductivity in the x-, y-, and z-directions, respectively. (d) The IC($\boldsymbol{k}$) function of $\tau\eta^{x}_{zx}$ at photon energy $\hbar\omega = 2.25$ eV. (e) The IC($\boldsymbol{k}$) of $\tau\eta^{y}_{zx}$ at $\hbar\omega = 2.16$ eV. (f) The IC($\boldsymbol{k}$) of $\tau\eta^{z}_{xy}$ at $\hbar\omega = 1.62$ eV.

integrated function of the IC photoconductivity, $\mathrm{IC}(\boldsymbol{k}) = \mathrm{Im}\left\{-\sum_{n,m} f_{nm}\Delta^{a}_{nm}[r^{b}_{mn}, r^{c}_{nm}]\delta(\omega_{mn}-\omega)\right\}$, as shown in Fig. 3(d)–(f). For the IC in the x-direction, $\hbar\omega = 2.25$ eV and $\tau\eta^{x}_{zx} = 101.1$ μA V^{-2}, and the main contribution solely comes from near the Γ point, as shown in Fig. 3(d). In the y-direction, $\hbar\omega = 2.16$ eV and $\tau\eta^{y}_{zx} = 132.4$ μA V^{-2}, and the main contributions are not only from near Γ but also from near the K and K' points, as illustrated in Fig. 3(e). Interestingly, for the IC in the z-direction, C_3 point group symmetry, $\tau\eta^{z}_{xy} = -\tau\eta^{z}_{yx} \neq 0$. The symmetry constraint does not lead to the disappearance of IC in the z-direction under CPL-xy. However, the calculated result $\tau\eta^{z}_{xy} \sim 10^{-5}$ μA V^{-2} is small enough to be negligible, as shown in Fig. 3(c). Further validation of this conclusion can be obtained from the IC($\boldsymbol{k}$) function of $\tau\eta^{z}_{xy}$, where IC($\boldsymbol{k}$) $\sim 10^{-4}$ Å^3, as shown in Fig. 3(f).

According to eqn (6) and (7), we can infer that SC is determined by the shift vector and transition rate, while IC is determined by the velocity difference and Berry curvature. We plotted the distribution of physical quantities in $\boldsymbol{k}$-space for SC and IC photoconductivities, as shown in Fig. S6.† All ferroic phases of CIPS are preserved in T-symmetry. The transformation rules of physical quantities under P-symmetry and T-symmetry are summarized in Table S4.†

It is known that P-symmetry leads to the disappearance of the BPVE, while T-symmetry has no effect. The change in physical quantities can verify this argument. Under P-symmetry, $Pv_{mn}(\boldsymbol{k}) = -v_{mn}(-\boldsymbol{k})$, $Pr_{nm}r_{mn}(\boldsymbol{k}) = r_{nm}r_{mn}(-\boldsymbol{k})$, $PR_{nm}(\boldsymbol{k}) = -R_{nm}(-\boldsymbol{k})$, $P\Delta_{mn}(\boldsymbol{k}) = -\Delta_{mn}(-\boldsymbol{k})$, and $P\Omega_{mn}(\boldsymbol{k}) = \Omega_{mn}(-\boldsymbol{k})$, where $R_{nm}r_{nm}r_{mn}$ and $\Delta_{mn}\Omega_{mn}$ are both odd functions. Therefore, under P-symmetry, both SC and IC vanish.

3.3 The BPVE during the phase transition

The SC and IC during the phase transition of CIPS: in the CIPS structure, with the movement of Cu and In atoms, opposite polarization FE2 phases and non-polar PE and AFE phases emerge. We calculated all SC and IC in various ferroic phases, and the photoconductivity of the FE2 phase is shown in Fig. S7,† PE phase in Fig. S8,† and AFE phase in Fig. S9.† Surprisingly, we found that CIPS ferroelectric property variations will lead to many intriguing nonlinear effects. In the opposite polarization FE2 phase, a portion of the photocurrent remains unchanged, while another part of the photocurrent undergoes a reversal, despite FE2 maintaining C_3 point group symmetry. In non-polar PE and AFE phases, some currents that exist in the ferroelectric phase become very small, while some currents that did not exist appear. We are very interested in this switching of photocurrent induced by ferroelectric properties, which is crucial for the application of ferroelectric materials in nonlinear optoelectronics.

The photocurrent during the phase transition from FE1 to FE2: we can observe from Fig. S7† that the polarization direction flips, σ^{x}_{xx}, σ^{z}_{xx}, σ^{z}_{zz} and $\eta^{x}_{zx} = -\eta^{y}_{yz}$, also undergo a reversal, while σ^{y}_{xx} and $\eta^{x}_{yz} = \eta^{y}_{zx}$ remain unchanged. To investigate the coupling between ferroelectric properties and photocurrent, we employed the climbing image nudged elastic band (CI-NEB) method to explore the structural and photocurrent evolution during the phase transition process. The structural evolution during the CI-NEB process is depicted in Fig. 4(a), with the initial state as the 00/FE1 structure (or image), transition state as 05/PE, and final state as 10/FE2. The CI-NEB path for the FE1 to FE2 phase transition is depicted in Fig. S10(a);† the phase

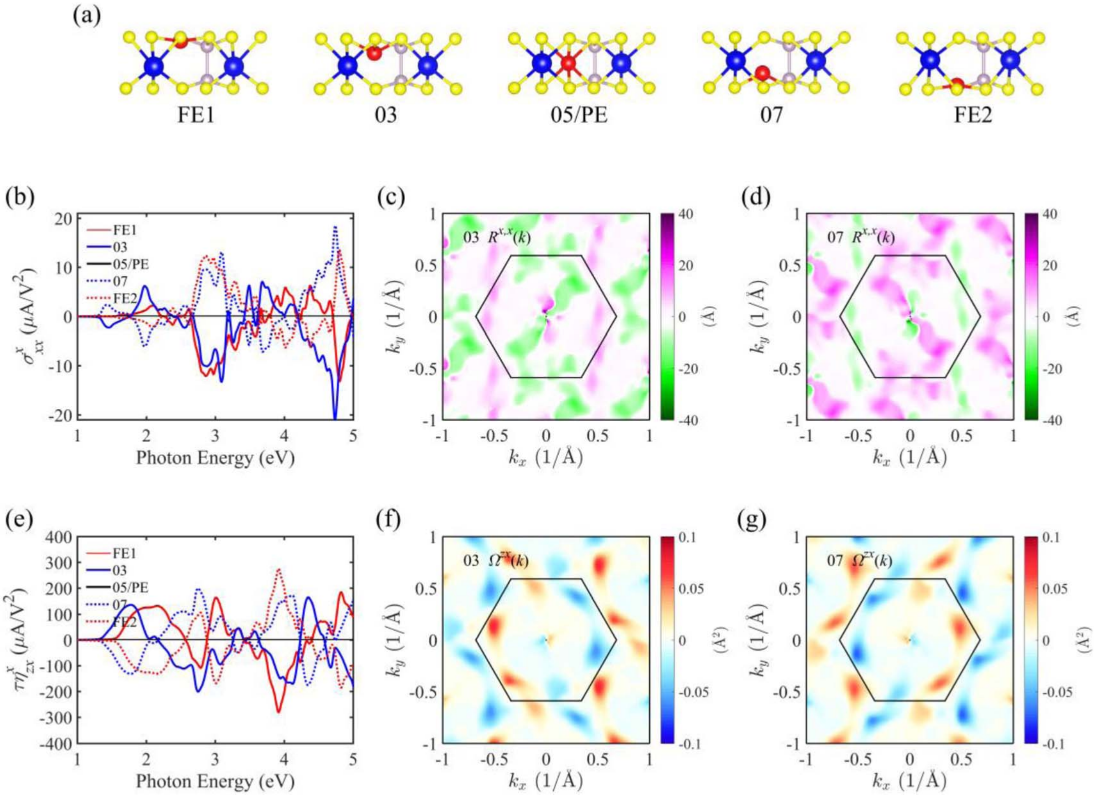

Fig. 4 The evolution of structure and photoconductivity during the phase transition from FE1 to FE2. (a) The evolution of the atomic structure during the phase transition. (b) The SC σ^x_{xx} during the phase transition. (c) and (d) The shift vector $R^{x,x}(\boldsymbol{k})$ of σ^x_{xx} in the structures 03 and 07, respectively. (e) The IC $\tau\eta^x_{zx}$ during the phase transition. (f) and (g) The Berry curvature $\Omega^{zx}(\boldsymbol{k})$ of $\tau\eta^x_{zx}$ in the structures 03 and 07, respectively.

transition barrier is only 339 meV and the structural transition is easily achievable under an external field.[39–41]

We illustrate photocurrent reversal with examples SC σ^x_{xx} and IC $\tau\eta^x_{zx}$, as shown in Fig. 4(b) and (e), respectively. The photoconductivity of all structures during the CI-NEB process can be found in Fig. S11.† The photoconductivities σ^x_{xx} and $\tau\eta^x_{zx}$ increase from FE1 to 03, decrease from 04 to 05/PE, completely disappear at 05/PE, and reverse the 05/PE to FE2 trend. We can observe from Fig. S11(a) and (e)† that the currents have opposite directions for 02 and 08 (03 and 07, 04 and 06). In the PE phase, $\sigma^x_{xx} = 0$ and $\tau\eta^x_{zx} = 0$, which is due to in-plane two-fold rotational symmetry. For photocurrents that do not change the direction with polarization reversal, we illustrate this with examples of SC σ^y_{xx} and IC $\tau\eta^y_{zx}$, as shown in Fig. S11(b) and (f),† respectively. They gradually increase from FE1 to 05/PE, reach a maximum at 05/PE, and gradually decrease from 05/PE to FE2. We can observe that the photoconductivities for 02 and 08 (03 and 07, 04 and 06) completely overlap. In the PE phase with D_3 point group symmetry, $\sigma^y_{xx} \neq 0$ and $\tau\eta^y_{zx} \neq 0$, and the maximum photoconductivity can reach $\tau\eta^y_{zx} = 809$ μA V^{-2} at $\hbar\omega = 4.9$ eV.

For a more in-depth understanding of the microscopic origins of photocurrent switching induced by the ferroelectric order, we charted the distribution of physical quantities in $\boldsymbol{k}$-space for photoconductivity, including the shift vector, transition rate, group velocity difference, and Berry curvature. For SC σ^x_{xx}, the shift vector $R^{x,x}(\boldsymbol{k})$ in structures 03 and 07 is shown in Fig. 4(c) and (d), and the transition rate $r^x r^x(\boldsymbol{k})$ is illustrated in Fig. S12(a) and (b).† We can infer from the distribution that the reversal of the ferroelectric order leads to a shift vector sign reversal, causing photocurrent switch. The shift vector of 07 is obtained by performing a mirror M_{ky} symmetry operation on the shift vector of 03; the mirror M_{ky} symmetry is perpendicular to k_y, and the shift vector signal undergoes inversion. Conversely, the transition rate also exhibits mirror M_{ky} symmetry operation, but the signal remains unchanged. In the PE phase, $\sigma^x_{xx} = 0$; the shift vector and transition rates are shown in Fig. S12(c) and (d).† It is clear that the shift vectors of 05/PE are mirror M_y anti-symmetric, while the transition rates are mirror symmetric. Therefore, integration over the first Brillouin zone is zero, resulting in $\sigma^x_{xx} = 0$.

For IC $\tau\eta^x_{zx}$, the Berry curvature $\Omega^{zx}(\boldsymbol{k})$ distribution of structures 03 and 07 is shown in Fig. 4(f) and (g), while the velocity difference is illustrated in Fig. S13(a) and (b).† From the distribution, we can observe that the reversal of the ferroelectric order leads to a sign reversal of the Berry curvature. We found that applying a mirror M_{ky} symmetry operation to the Berry curvature of 03 and adding a negative sign result in the Berry curvature of 07. For the velocity difference $\Delta^x(\boldsymbol{k})$ and Berry curvature $\Omega^{zx}(\boldsymbol{k})$ of 05/PE, as shown in Fig. S13(c) and (d),† the velocity difference is mirror M_{ky} symmetric and Berry curvature is mirror M_{ky} anti-symmetric, thus $\tau\eta^x_{zx} = 0$.

The phase transition from FE1 to AFE: the photoconductivity of the AFE phase is depicted in Fig. S9.† As ferroelectricity transforms into antiferroelectricity, σ^x_{xx}, σ^z_{xx}, σ^z_{zz}, $\tau\eta^x_{zx}$ and

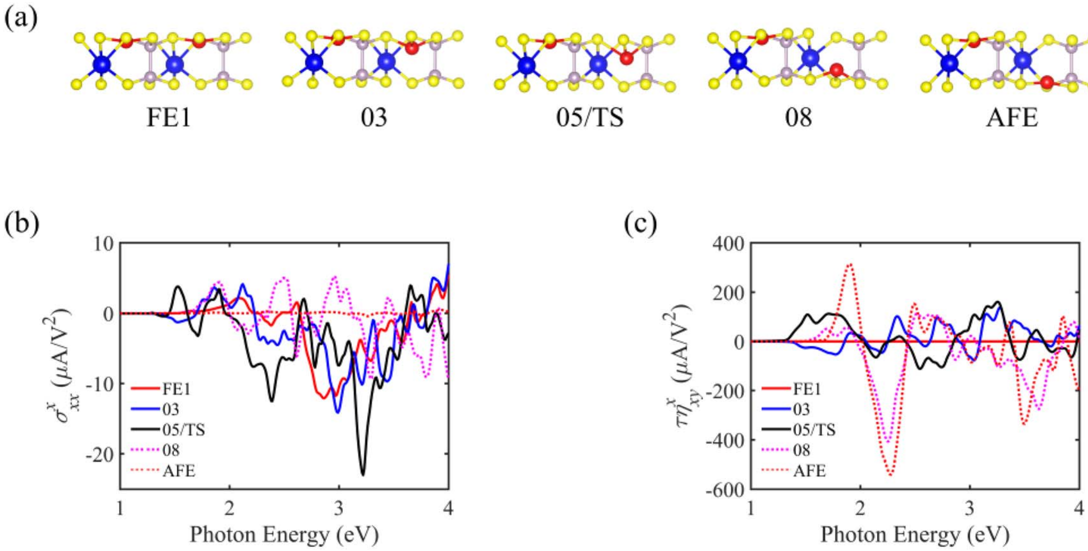

Fig. 5 The evolution of structure and photoconductivity during the phase transition from FE1 to AFE. (a) The evolution of the atomic structure during the phase transition. (b) The SC σ^x_{xx} during the phase transition. (c) The IC $\tau\eta^x_{xy}$ during the phase transition.

$\tau\eta^y_{yz}$ decrease, whereas $\tau\eta^x_{xy}$ and σ^y_{zz} are no longer zero. The CI-NEB path for the FE1 to AFE transition is illustrated in Fig. S10(b),† with the initial state as the 00/FE1 structure and the final state as the 10/AFE structure. The transition barrier is only 281.1 meV. The atomic structure evolution during the CI-NEB process is depicted in Fig. 5(a). The point group of the AFE phase is C_1, with the lowest symmetry, resulting in all conductivity elements being non-zero. An interesting discovery is that the larger currents in the ferroelectric phase become very small in the AFE phase, while the currents that vanish in the ferroelectric phase due to symmetry constraints reappear with significant values in the AFE phase. Here, we illustrate the trends by taking SC σ^x_{xx} and IC $\tau\eta^x_{xy}$ as examples, as shown in Fig. 5(b) and (c), respectively. Other components, such as σ^z_{xx} and $\tau\eta^y_{yz}$, exhibit similar trends, as detailed in Fig. S14.† For the SC σ^x_{xx}, it gradually increases from FE1 to 05/TS, reaching its maximum at 05/TS, and then decreases gradually from 05/TS to AFE, where the photocurrent in AFE becomes negligible. For the IC $\tau\eta^x_{xy}$, it increases gradually from FE1 to AFE, reaching its maximum at AFE, with $\hbar\omega = 2.28$ eV and $\tau\eta^x_{xy} = -540$ μA V^{-2}. In FE1/FE2 and PE phases, $\tau\eta^x_{xy} = 0$ due to symmetry constraints. However, during the FE1 to AFE phase transition, small displacements of neighboring Cu atoms (*e.g.*, 02) lead to the appearance of a signal in $\tau\eta^x_{xy}$.

3.4 Manipulating nonlinear photo-responsivity

Developing effective strategies to manipulate nonlinear photo-responsivity is crucial for the practical applications of materials in nonlinear optics. The electronic properties of materials can be controlled through external stimuli, such as doping, strain, and electric fields, to achieve control over nonlinear photo-responsivity.[43–45] First, we explored the impact of chalcogen element substitution in CIPS on SC and IC. We calculated the photoconductivity of CIPX (X = S, Se, Te) in the FE1 phase, as shown in Fig. 6. It is observed that with the increasing atomic number of chalcogen elements (*i.e.*, from S to Se and Te), the photocurrent also increases, with CIPTe generally exhibiting the highest photoconductivity. This finding can be explained by the earlier electronic band structure analysis, where a larger atomic number of chalcogen elements leads to a smaller band gap, favoring the photoexcitation of charge carriers and resulting in a larger photoconductivity. Regarding the BPVE in CIPTe, for shift current, $\sigma^x_{xx} = 55.3$ μA V^{-2} (at photon energy $\hbar\omega = 0.54$ eV) and $\sigma^y_{xx} = -40.4$ μA V^{-2} ($\hbar\omega = 0.55$ eV); for injection current, $\tau\eta^x_{zx} = -514.6$ μA V^{-2} ($\hbar\omega = 3.21$ eV) and $\tau\eta^y_{zx} = 513.5$ μA V^{-2} ($\hbar\omega$ = 2.7 eV). Device design highly desires materials with strong nonlinear optical responses. The photoconductivity of common 2D semiconductor materials such as BN, TMDs (MoS$_2$),[32,33] *etc.*, is in the range of 10–10^2 μA V^{-2}, while the response intensity of CIPX (X = S, Se, Te) is several times that of these materials.

Similar to CIPS, we observe ferroelectric order induced photocurrent switching in CIPSe and CIPTe. The CI-NEB path for the FE1 to FE2 phase transition in CIPSe and CIPTe is shown in Fig. S15(a) and (b),† with transition barriers of 171.8 meV and 118.7 meV, respectively. We calculated the SC and IC photoconductivities for the FE1, FE2, PE, and AFE phases of CIPSe (CIPTe), as shown in Fig. S16 and S17.† We can see that CIPSe (CIPTe) exhibits similar results to CIPS, due to their identical structural symmetry.

The SC and IC under strain engineering: for concise illustration, we take the FE1 phase of CIPS as an example, applying biaxial strain in the plane. The total energy of FE1, PE, and AFE phases of CIPS as a function of strain is shown in Fig. 7(a). The unit cell of the AFE phase is twice that of the FE1 (PE) phase, so we need to consider half of the total energy for AFE for comparison. The total energy variations for CIPSe and CIPTe are depicted in Fig. S18(a) and (b).† We found that after applying strain, the ground state with the lowest total energy for CIPS, CIPSe, and CIPTe retains the AFE phase. Fig. 7(b) illustrates the relationship between the band gap and strain. The band gap

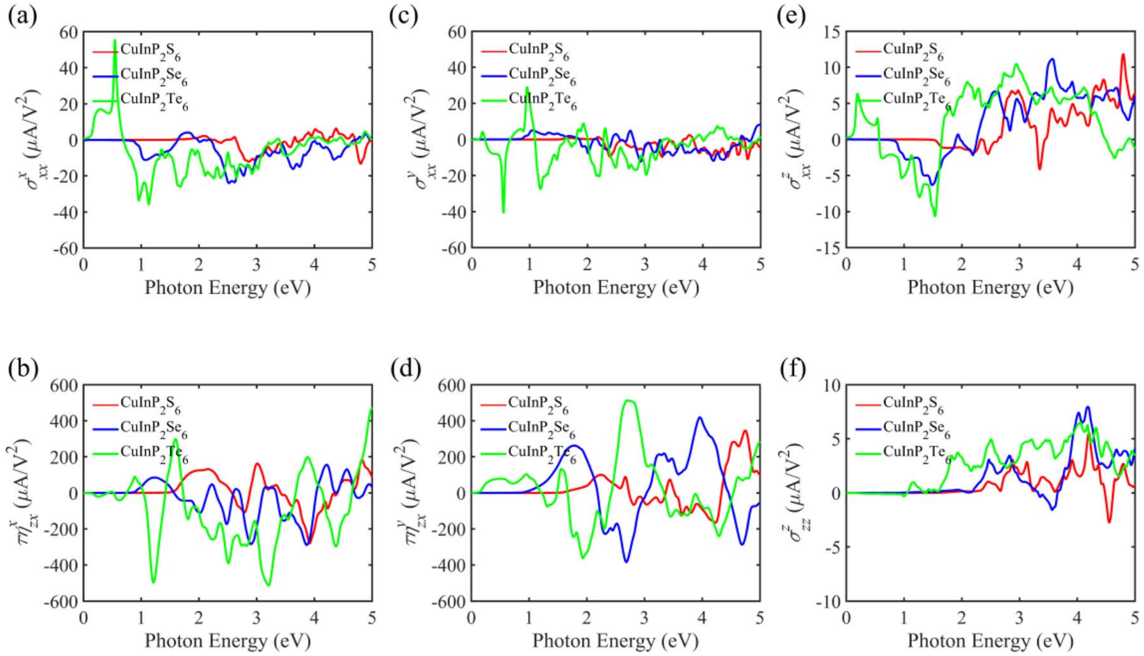

Fig. 6 The SC and IC photoconductivities of CIPX (X = S, Se, and Te) in the FE1 phase. (a) σ^x_{xx}. (b) $\tau\eta^x_{zx}$. (c) σ^y_{xx}. (d) $\tau\eta^y_{zx}$. (e) σ^z_{xx}. (f) σ^z_{zz}.

increases under compressive strain, then slightly decreases (>−5%), and linearly decreases under tensile strain.

Fig. 7(c) and (e) show the SC σ^y_{xx} under compressive and tensile strain, respectively. Other components, such as SC σ^x_{xx}, σ^z_{xx}, and σ^z_{zz} and IC $\tau\eta^y_{zx}$ are detailed in Fig. S19.† We observe that under compressive strain, the SC photoconductivity decreases, and the peak undergoes a blue shift, marked with circles in the figure. Conversely, under tensile strain, the photoconductivity increases, and the peak undergoes a red shift. The IC $\tau\eta^x_{zx}$ follows a similar trend, as shown in Fig. 7(d) and (f). Typically, applying in-plane compressive strain will increase the vertical thickness of 2D materials, leading to an

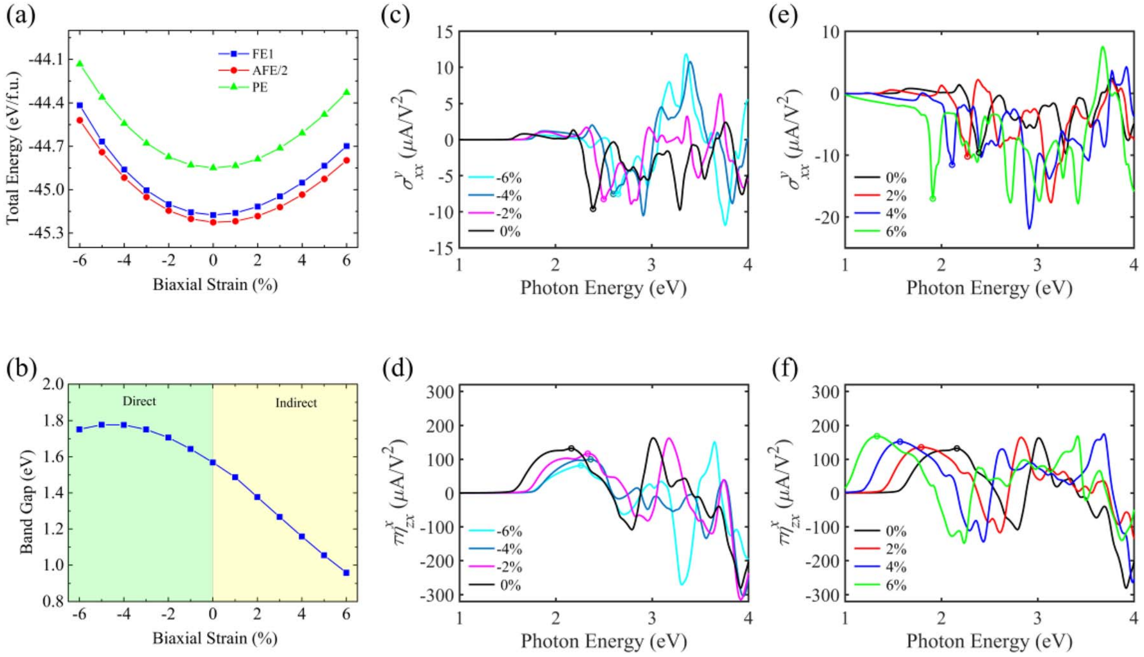

Fig. 7 The SC and IC photoconductivities under in-plane biaxial strain. (a) The total energy of CIPS in the FE1, PE, and AFE phases as a function of strain. (b) The band gap variation of CIPS in the FE1 phase under strain, with the green region indicating the direct band gap and the yellow region indicating the indirect band gap. (c) and (e) The SC σ^y_{xx} under compressive and tensile strain, respectively. (d) and (f) The IC $\tau\eta^x_{zx}$ under compressive and tensile strain, respectively.

increased vertical distance between Cu and In atoms. Conversely, applying tensile strain reduces the thickness, bringing Cu and In atoms closer to each other. The change in the distance between Cu and In atoms affects the ferroelectric and electronic properties of CIPS. Tensile strain reduces the direct band gap of CIPS, bringing the valence and conduction bands closer, facilitating carrier transitions. This results in an enhancement of the photocurrent and a red shift, whereas compressive strain induces a blue shift.

3.5 Discussion

Before concluding, some interesting findings merit further discussion. In the CIPX (X = S, Se, Te) system, we observe that the reversal of photocurrent can be achieved not only by changing the chirality of polarized light but also by altering the ferroelectric properties. In the FE phase, the photocurrent switches under polarized light, for SC, $\sigma^x_{xx} = -\sigma^x_{yy}$ and $\sigma^y_{xx} = -\sigma^y_{yy}$, and for IC, $\tau\eta^x_{yz} = -\tau\eta^y_{xz}$ and $\tau\eta^x_{zx} = -\tau\eta^y_{yz}$, as determined by the structural symmetry. In the PE phase, $\sigma^y_{xx} = -\sigma^y_{yy}$ and $\tau\eta^x_{yz} = -\tau\eta^y_{xz}$, due to D_3 point group symmetry. However, for IC, $\tau\eta^x_{yz} = -\tau\eta^x_{zy}$, caused by the commutation relation in Berry curvature is an intrinsic property achievable in any material. The photocurrent switches by the ferroelectric order: despite FE1 and FE2 sharing the same structural symmetry, the polarization direction can induce photocurrent reversal, such as σ^x_{xx}, σ^z_{xx}, σ^z_{zz}, and $\tau\eta^x_{zx}$. The microscopic mechanism behind this is the opposite sign of physical quantities in photoconductivity. This rich coupling between nonlinear optics and structural symmetry, as well as ferroelectric ordering, provides powerful tools for studying photon excitation in ferroelectric materials, characterizing structural phase transitions, and imaging ferroelectric domains.

Recently, researchers have discovered thousands of ferroelectric materials with the same configuration as CIPS through high-throughput first-principles calculations and data-driven machine learning methods.[46] These materials, denoted as $M_I M_{II} P_2 X_6$, consist of different metal elements M_I and M_{II} and the chalcogen atom X. The structural predictions open up possibilities for various applications of ferroelectric materials. It is hoped that these materials exhibit strong nonlinear optical responses. However, individually computing the nonlinear optical response for each structure is a massive task. Therefore, a universal theoretical framework for predicting larger photocurrents necessitates further exploration.

Additionally, the successful experimental synthesis of the two-dimensional layered $CuCrP_2S_6$ structure has been achieved recently.[47] Similar structures such as $CuMP_2X_6$ (M = Cr, V; X = S, Se) have also attracted significant attention.[48] This material coexists with ferroelectric, ferromagnetic and ferrovalley materials as a multiferroic material, where Cr and V atoms provide the magnetism. In multiferroic materials, the presence of magnetism breaks *T*-symmetry. The theoretical framework for the bulk photovoltaic effect used in this work is no longer applicable in the presence of both *P*- and *T*-symmetry breaking. Therefore, it becomes necessary to simultaneously consider *P*- and *T*-symmetry breaking. The complex interplay between multiferroicity and nonlinear optics induces novel physical effects and diverse applications. Understanding the intricate microscopic mechanisms in these systems requires deeper exploration by researchers.

4. Conclusion

In summary, we employed first-principles calculations and nonlinear response theory to investigate the BPVE in a 2D room-temperature ferroelectric material CIPS. Due to variations in structural symmetries, notable distinctions arise in the nonlinear photo-responsivity of CIPS across its distinct ferroic phases, such as in the FE phase, $\sigma^x_{xx} = -\sigma^x_{yy}$, in the PE phase, $\sigma^x_{xx} = 0$ and $\sigma^x_{yy} = 0$, and in the AFE phase, $\sigma^x_{xx} \neq \sigma^x_{yy} \neq 0$. We discovered that the chirality of polarized light can switch the photocurrent in both the FE and PE phases, while the AFE phase exhibits the lowest structural symmetry, with all conductivity tensors being independent and non-zero. By analyzing the evolution of photocurrent during FE1 to FE2 phase transition processes, we discover that the reversal of ferroelectric ordering can induce a photocurrent flip, such as σ^x_{xx}, σ^z_{xx}, σ^z_{zz}, and $\tau\eta^x_{zx}$, attributed to the sign change of topological physical quantities such as the shift vector and Berry curvature. Additionally, during the polar to non-polar transition from FE1 to AFE, σ^x_{xx}, σ^z_{xx}, σ^z_{zz}, $\tau\eta^x_{zx}$ and $\tau\eta^y_{yz}$ decrease, whereas $\tau\eta^x_{xy}$ and σ^y_{zz} are no longer zero. Furthermore, our investigation reveals that chalcogen element substitution (CIPX, where X = S, Se, Te) and strain engineering can effectively modulate the BPVE. Specifically, a narrower band gap favors electron excitation, resulting in enhanced photocurrent. Our work holds significant importance in understanding the switchable BPVE in ferroelectric materials and paves a novel path for the practical applications of the excellent room-temperature ferroelectric material CIPS.

5. Computational methods

First-principles calculations were performed based on density functional theory (DFT) using the VASP.[49,50] The generalized gradient approximation (GGA) with Perdew–Burke–Ernzerhof (PBE) pseudopotentials was employed to examine the exchange–correlation interactions between electrons.[51] The wavefunctions were expanded using the projected augmented wave (PAW) method,[52] with a plane wave cutoff energy of 520 eV. The atomic structures underwent full relaxation, with the energy convergence set to 10^{-6} eV and an interatomic force convergence accuracy of 10^{-2} eV Å^{-1}. The reciprocal space was sampled using a Γ centered *k*-mesh, with a grid density of $2\pi \times 0.02$ Å^{-1}. For the FE and PE phases, a *k*-mesh of 9 × 9 × 1 was employed, while for the AFE phase, a *k*-mesh of 9 × 5 × 1 was used. To avoid interference from periodic interactions between adjacent layers in the *z*-direction for 2D materials, the thickness of the vacuum layer in the supercell was set to be no less than 15 Å. All calculations considered the effects of spin–orbit coupling (SOC). The phonon spectrum was calculated using the density functional perturbation theory (DFPT) method with a 4 × 4 × 1 supercell.

5.1 Nonlinear photo-responsivity calculations

We employed maximally localized Wannier functions (MLWF) to construct the tight-binding (TB) Hamiltonian for all systems, using the Wannier90 program.[53,54] To address gauge issues, we utilized the TB Hamiltonian to compute all matrix elements for SC and IC conductivity. We projected the Cu 3d, 4s; In 5s, 5p; P 3s, 3p; and S (Se, Te) 3p atomic orbitals based on the distribution of projected energy bands near the Fermi level. A total of 72 Wannier functions were projected. Considering that deep energy level electrons are difficult to excite, we chose to project 44 bands onto the valence bands near the Fermi level and 28 bands onto the conduction bands. Finally, to ensure the accuracy of the TB Hamiltonian, we compared the band structures obtained from Wannier and GGA-PBE calculations, and the results demonstrated excellent agreement between TB and DFT bands, as shown in Fig. S1(c).†

Diagonalizing the TB Hamiltonian H^W at each $\boldsymbol{k}$-point, one obtains the wavefunctions $|n_k\rangle^W$ and energies $E_n{}^W(k)$ for each band at $\boldsymbol{k}$-points.

Velocity matrix,

$$v_{mn}^a = \left\langle m_k \middle| \frac{\partial H^W}{\partial k_a} \middle| n_k \right\rangle^w$$

Berry connection matrix,

$$r_{mn}^a = -\frac{i\hbar}{E_m{}^W(k) - E_n{}^W(k)} \left\langle m_k \middle| \frac{\partial H^W}{\partial k_a} \middle| n_k \right\rangle^W (m \neq n)$$

Dirac delta function,

$$\delta(\omega_{mn} - \omega) = \lim_{\varepsilon \to 0} \frac{1}{\pi} \frac{\varepsilon}{\varepsilon^2 + (\omega_{mn} - \omega)^2}$$

where ε is the broadening factor, and it can be treated as $\varepsilon = \frac{\hbar}{e \cdot \tau/(2\pi)}$. For the carrier lifetime, we used a conservative constant value $\tau = 0.2$ ps, with the broadening factor approximately being $\varepsilon = 0.02$ eV.

The integration of conductivity over the entire $\boldsymbol{k}$-space is transformed into a weighted sum, $\int_{BZ} I(k) \frac{d^3k}{(2\pi)^3} = \frac{1}{V} \sum_k w_k I(k)$. Here, $I(\boldsymbol{k})$ represents the integration function, V is the volume of the unit cell, and $w_{\boldsymbol{k}}$ is the weighting factor. When calculating the photoconductivity of two-dimensional materials, the integration function $I(\boldsymbol{k})$ along the z-direction is not meaningful, so $\partial z = 1$ should be used. In the convergence test of k-point sampling density for photoconductivity calculations, the $641 \times 641 \times 1$ k-mesh used in this paper has reached convergence, as shown in Fig. S1(d).† In order to ensure that the conductivity calculated from the supercells of 2D materials (σ_{slab}) is comparable to that of conventional bulk materials, we introduce a scaling factor, $\sigma_{\text{2D}} = \frac{L_z}{L_{\text{eff}}} \sigma_{\text{slab}}$, where L_z denotes the lattice parameter along the z-direction of the unit cell and L_{eff} represents the effective thickness. Based on the structural parameters of bulk CIPS,[55] the effective thickness corresponds to the interlayer distance, $L_{\text{eff}} = 6.6$ Å, and computed results presented in this paper are all for the σ_{2D} conductivity.

Additionally, we considered the effect of dipole corrections on the photocurrent in ferroelectric materials, as shown in Fig. S1(e).† The inclusion of dipole corrections has a minimal impact on the calculated results, and the results presented in this paper do not include dipole corrections. Moreover, we tested the effect of carrier lifetime τ on SC and IC, as shown in Fig. S1(f).† We found that SC is generated instantaneously, and SC photoconductivity shows no correlation with carrier lifetime. For IC, it initially grows with time and reaches saturation in the static limit, where IC photoconductivity is proportional to the carrier lifetime.

Data availability

The original data supporting the findings of this study are available from the corresponding author upon reasonable request.

Author contributions

Yu-Jun Zhao and Chengwei Liao conceived the idea and designed the project. Chengwei Liao performed the calculations. Chengwei Liao, Minglong Wang, and Yu-Jun Zhao analyzed the results. Yu-Jun Zhao supervised the project. Yu-Jun Zhao and Chengwei Liao developed the first-principles codes for computing second-order nonlinear photocurrent and wrote the manuscript.

Conflicts of interest

There are no conflicts to declare.

Acknowledgements

This work was financially supported by National Natural Science Foundation of China (Grant No. 12074126). The computer time at the High Performance Computational Center at South China University of Technology is gratefully acknowledged.

References

1 A. M. Glass, D. von der Linde and T. J. Negran, *Appl. Phys. Lett.*, 1974, **25**, 233.

2 I. Grinberg, D. V. West, M. Torres, G. Gou, D. M. Stein, L. Wu, G. Chen, E. M. Gallo, A. R. Akbashev, P. K. Davies, J. E. Spanier and A. M. Rappe, *Nature*, 2013, **503**, 509–512.

3 X. Jiang, L. Kang, J. Wang and B. Huang, *Phys. Rev. Lett.*, 2023, **130**, 256902.

4 J. W. McIver, D. Hsieh, S. G. Drapcho, D. H. Torchinsky, D. R. Gardner, Y. S. Lee and N. Gedik, *Phys. Rev. B: Condens. Matter Mater. Phys.*, 2012, **86**, 035327.

5 Z. Sun, Y. Yi, T. Song, G. Clark, B. Huang, Y. Shan, S. Wu, D. Huang, C. Gao, Z. Chen, M. McGuire, T. Cao, D. Xiao,

W. T. Liu, W. Yao, X. Xu and S. Wu, *Nature*, 2019, **572**, 497–501.

6 S. Yang, J. Seidel, S. Byrnes, P. Shafer, C. H. Yang, M. D. Rossell, P. Yu, Y. H. Chu, J. F. Scott, J. W. Ager lll, L. W. Martin and R. Ramesh, *Nat. Nanotechnol.*, 2010, **5**, 143–147.

7 J. E. Spanier, V. M. Fridkin, A. M. Rappe, A. R. Akbashev, A. Polemi, Y. Qi, Z. Gu, S. M. Young, C. J. Hawley, D. Imbrenda, G. Xiao, A. L. Bennett-Jackson and C. L. Johnson, *Nat. Photonics*, 2016, **10**, 611.

8 Y. J. Zhang, T. Ideue, M. Onga, F. Qin, R. Suzuki, A. Zak, R. Tenne, J. H. Smet and Y. Iwasa, *Nature*, 2019, **570**, 349–353.

9 G. B. Osterhoudt, L. K. Diebel, M. J. Gray, X. Yang, J. Stanco, X. Huang, B. Shen, N. Ni, P. J. W. Moll, Y. Ran and K. S. Burch, *Nat. Mater.*, 2019, **18**, 471–475.

10 M. Zhao, Z. Ye, R. Suzuki, Y. Ye, H. Zhu, J. Xiao, Y. Wang, Y. Iwasa and X. Zhang, *Light: Sci. Appl.*, 2016, **5**, e16131.

11 H. Wang and X. Qian, *Sci. Adv.*, 2019, **5**, eaav9743.

12 S. M. Young and A. M. Rappe, *Phys. Rev. Lett.*, 2012, **109**, 116601.

13 X. Mu, Y. Pan and J. Zhou, *npj Comput. Mater.*, 2021, **7**, 61.

14 Z. Qian, J. Zhou, H. Wang and S. Liu, *npj Comput. Mater.*, 2023, **9**, 67.

15 L. Ye, W. Zhou, D. Huang, X. Jiang, Q. Guo, X. Cao, S. Yan, X. Wang, D. Jia, D. Jiang, Y. Wang, X. Wu, X. Zhang, Y. Li, H. Lei, H. Gou and B. Huang, *Nat. Commun.*, 2023, **14**, 5911.

16 W. Zhong, R. D. King-Smith and D. Vanderbilt, *Phys. Rev. Lett.*, 1994, **72**, 3618.

17 J. Junquera and P. Ghosez, *Nature*, 2003, **422**, 506–509.

18 M. Stengel, N. Spaldin and D. Vanderbilt, *Nat. Phys.*, 2009, **5**, 304–308.

19 H. Wang and X. Qian, *2D Mater.*, 2017, **4**, 015042.

20 C. Xiao, F. Wang, S. A. Yang, Y. Lu, Y. Feng and S. Zhang, *Adv. Funct. Mater.*, 2018, **28**, 1707383.

21 Z. Fei, W. Zhao, T. A. Palomaki, B. Sun, M. K. Miller, Z. Zhao, J. Yan, X. Xu and D. H. Cobden, *Nature*, 2018, **560**, 336–339.

22 C. Cui, W. J. Hu, X. Yan, C. Addiego, W. Gao, Y. Wang, Z. Wang, L. Li, Y. C. Cheng, P. Li, X. Zhang, H. N. Alshareef, T. Wu, W. Zhu, X. Pen and L. J. Li, *Nano Lett.*, 2018, **18**, 1253–1258.

23 X. Meng, Y. Shen, J. Liu, L. Lv, M. Zhou, X. Yang, Y. Zhang and Z. Zhou, *Appl. Surf. Sci.*, 2023, **638**, 158084.

24 A. Belianinov, Q. He, A. Dziaugys, P. Maksymovych, E. Eliseev, A. Borisevich, A. Morozovska, J. Banys, Y. Vysochanskii and S. V. Kalinin, *Nano Lett.*, 2015, **15**, 3808–3814.

25 F. Liu, L. You, K. Seyler, X. Li, P. Yu, J. Lin, X. Wang, J. Zhou, H. Wang, H. He, S. T. Pantelides, W. Zhou, P. Sharma, X. Xu, P. M. Ajayan, J. Wang and Z. Liu, *Nat. Commun.*, 2016, **7**, 12357.

26 W. Huang, F. Wang, L. Yin, R. Cheng, Z. Wang, M. G. Sendeku, J. Wang, N. Li, Y. Yao and J. He, *Adv. Mater.*, 2020, **32**, 1908040.

27 M. Si, P. Y. Liao, G. Qiu, Y. Duan and P. D. Ye, *ACS Nano*, 2018, **12**, 6700–6705.

28 H. Liu, S. Yu, Y. Wang, B. Huang, Y. Dai and W. J. Wei, *J. Phys. Chem. Lett.*, 2022, **13**, 1972–1978.

29 W. Kraut and R. von Baltz, *Phys. Rev. B: Condens. Matter Mater. Phys.*, 1979, **19**, 1548–1554.

30 R. von Baltz and W. Kraut, *Phys. Rev. B: Condens. Matter Mater. Phys.*, 1981, **23**, 5590–5596.

31 J. E. Sipe and A. I. Shkrebtii, *Phys. Rev. B: Condens. Matter Mater. Phys.*, 2000, **61**, 5337–5352.

32 H. Xu, H. Wang, J. Zhou and J. Li, *Nat. Commun.*, 2021, **12**, 4330.

33 H. Xu, H. Wang, J. Zhou, Y. Guo, J. Kong and J. Li, *npj Comput. Mater.*, 2021, **7**, 31.

34 H. Wang, C. Zhang and F. Rana, *Nano Lett.*, 2015, **15**, 8204.

35 L. Wu, M. Brahlek, R. Valdés Aguilar, A. V. Stier, C. M. Morris, Y. Lubashevsky, L. S. Bilbro, N. Bansal, S. Oh and N. P. Armitage, *Nat. Phys.*, 2013, **9**, 410.

36 G. B. Ventura, D. J. Passos, J. M. B. Lopes Dos Santos, J. M. Viana Parente Lopes and N. M. R. Peres, *Phys. Rev. B*, 2017, **96**, 035431.

37 A. Taghizadeh, F. Hipolito and T. G. Pedersen, *Phys. Rev. B*, 2017, **96**, 195413.

38 S. Jiang, H. Yin, J. Li, L. Liu, X. Shi, Y. Yan, C. Liu, G. P. Zhang and P. F. Liu, *Phys. Status Solidi RRL*, 2020, **14**, 2000321.

39 G. Yu, A. Pan and M. Chen, *Phys. Rev. B*, 2021, **104**, 224102.

40 Z. Z. Sun, W. Xun, L. Jiang, J. L. Zhong and Y. Z. Wu, *J. Phys. D: Appl. Phys.*, 2019, **52**, 465302.

41 D. D. Xu, R. R. Ma, A. P. Fu, Z. Guan, N. Zhong, H. Peng, P. H. Xiang and C. G. Duan, *Nat. Commun.*, 2021, **12**, 655.

42 R. W. Boyd, *Nonlinear Optics*, Elsevier Inc., 3rd edn, 2008.

43 A. Strasser, H. Wang and X. Qian, *Nano Lett.*, 2022, **22**, 4145–4152.

44 J. Jiang, Z. Chen, Y. Hu, Y. Xiang, L. Zhang, Y. Wang, G. C. Wang and J. Shi, *Nat. Nanotechnol.*, 2021, **16**, 894.

45 H. Wang and X. Qian, *npj Comput. Mater.*, 2020, **6**, 199.

46 X. Y. Ma, H. Y. Lyu, K. R. Hao, Y. M. Zhao, X. Qian, Q. B. Yan and G. Su, *Sci. Bull.*, 2021, **66**, 233–242.

47 M. A. Susner, R. Rao, A. T. Pelton, M. V. McLeod and B. Maruyama, *Phys. Rev. Mater.*, 2020, **4**, 104003.

48 D. Zhang, A. Li, X. Chen, W. Zhou and F. Ouyang, *Phys. Rev. B*, 2022, **105**, 085408.

49 W. Kohn and L. J. Sham, *Phys. Rev.*, 1965, **140**, A1133–A1138.

50 G. Kresse and J. Furthmüller, *Comput. Mater. Sci.*, 1996, **6**, 15–50.

51 J. P. Perdew, K. Burke and M. Ernzerhof, *Phys. Rev. Lett.*, 1996, **77**, 3865–3868.

52 P. E. Blöchl, *Phys. Rev. B: Condens. Matter Mater. Phys.*, 1994, **50**, 17953–17979.

53 N. Marzari, A. A. Mostofi, J. R. Yates, I. Souza and D. Vanderbilt, *Rev. Mod. Phys.*, 2012, **84**, 1419–1475.

54 A. A. Mostofi, J. R. Yates, G. Pizzi, Y. S. Lee, I. Souza, D. Vanderbilt and N. Marzari, *Comput. Phys. Commun.*, 2014, **185**, 2309–2310.

55 S. Zhou, L. You, H. Zhou, Y. Pu, Z. Gui and J. Wang, *Front. Phys.*, 2021, **16**, 13301.